American Mineralogist, Volume 87, pages 1662–1671, 2002

Structure of synthetic Na-birnessite: Evidence for a triclinic one-layer unit cell

BRUNO LANSON,[1,*] VICTOR A. DRITS,[1,2] QI FENG,[3] AND ALAIN MANCEAU[1]

[1]Environmental Geochemistry Group, LGIT, Maison des Géosciences, BP53, University of Grenoble - CNRS, 38041 Grenoble Cedex 9, France

[2]Geological Institute, Russian Academy of Sciences, 7 Pyzhevsky Street, 109017 Moscow, Russia

[3]Department of Advanced Materials Science, Faculty of Engineering, Kagawa University, 2217-20 Hayashi-cho, Takamatsu, Kagawa, 761-0396, Japan

ABSTRACT

The structure of a synthetic analogue of Na-birnessite (NaBi) was studied by powder X-ray diffraction (XRD). It is shown that NaBi has a one-layer triclinic structure with sub-cell parameters: a_P = 2.9513(4) Å, b_P = 2.9547(4) Å, c_P = 7.334(1) Å, α_P = 78.72(2)°, β_P = 101.79(1)°, γ_P = 122.33(1)°, and space group $P\bar{1}$. This sub-cell is equivalent to the base-centered sub-cell with parameters: a = 5.174 Å, b = 2.848 Å, c = 7.334 Å, α = 90.53°, β = 103.20°, and γ = 90.07°. A structure model has been refined using the Rietveld technique. NaBi consists of vacancy-free Mn-bearing octahedral layers whose negative charge arises mostly from the substitution of Mn^{3+} for Mn^{4+}. The departure from the hexagonal symmetry of layers results from Jahn-Teller distortion of Mn^{3+} octahedra, which are elongated along the **a** axis, segregated in Mn^{3+}-rich rows parallel to the **b** axis, and separated from each other along the **a** axis by two Mn^{4+}-rows. Structural sites of interlayer Na cations and H_2O have been determined as well as their occupancies. The sub-cells of the two NaBi modifications described by Drits et al. (1997) as types I and II likely contain four sites for interlayer species, two of which are occupied by Na and the other two by H_2O molecules. In the two NaBi varieties, these pairs of sites are split along the **c** axis and related by a center of symmetry. This splitting is consistent with the modulated structure of both NaBi types, which arises from the periodic displacement of interlayer species along the **b** axis with a periodicity $\lambda = 6b$ (Drits et al. 1997).

INTRODUCTION

Birnessite is the most common mineral of the phyllo-manganate family. It can form under a variety of physico-chemical conditions and is consequently present in different geological environments such as soils (Taylor et al. 1964; Chukhrov and Gorshkov 1981; Cornell and Giovanoli 1988), marine manganese nodules and micro-nodules (Burns and Burns 1976; Glover 1977; Chukhrov et al. 1978, 1985, 1989; Drits et al. 1985), and Mn-rich ore deposits (Usui and Mita 1995). Furthermore, birnessite possesses unique surface-charge (Healy et al. 1966; Murray 1974), cation-exchange (Balistrieri and Murray 1982; Le Goff et al. 1996), and redox (Stone et al. 1994) properties, which makes it highly reactive with respect to sorption phenomena (Paterson et al. 1994; Tu et al. 1994). It is also easily synthesized under laboratory conditions (Bricker 1965; Stälhi 1968; Giovanoli et al. 1970a, 1970b; Golden et al. 1986; Strobel et al. 1987; Cornell and Giovanoli 1988) and therefore has been often used as a model Mn oxide in environmental chemical studies (Stone and Morgan 1984; Stone 1987; Manceau and Charlet 1992; Xyla et al. 1992; Bidoglio et al. 1993).

Two major synthetic analogues of Na-birnessite (NaBi) have been described in the literature. A three-layer hexagonal modification was synthesized recently under hydrothermal conditions (Chen et al. 1996). However, the most common way to synthesize NaBi is through the formation of Na-rich 10 Å buserite at room temperature and high pH, which is then partially dehydrated to form NaBi (Giovanoli et al. 1970a; Feng et al. 1997). Post and Veblen (1990) determined for the first time the monoclinic one-layer sub-structure of this phyllomanganate using the Rietveld technique, together with transmission electron microscopy (TEM) and selected area electron diffraction (SAED). Drits et al. (1997), and Silvester et al. (1997), using SAED and extended X-ray absorption fine structure spectroscopy (EXAFS), further studied the structure and crystal chemistry of synthetic NaBi, concentrating on the nature and origin of its super-cell and modulated structures.

These authors did not perform any additional XRD analysis and assumed that the sub-structure determined by Post and Veblen (1990) was correct. However, the precision of refined structural parameters (atomic positions and occupancies) was not sufficient to allow a complete and unambiguous determination of all details of the NaBi sub-structure, even though its main structural and chemical properties were reasonably well-known. In particular, they were unable to draw definitive conclusions about the respective contributions of layer Mn^{3+} and/or layer vacancies to the layer charge. Accordingly, it was impossible from their results to choose unambiguously between the two structural formulae $Na^{1+}_{0.29}(Mn^{4+}_{0.71}Mn^{3+}_{0.29})O_2 \cdot 0.75H_2O$ and $Na^{1+}_{0.29}(Mn^{4+}_{0.93}\square_{0.07})O_2 \cdot 0.75H_2O$. Similarly, the position of the interlayer species could not be determined precisely because the O2 site on the difference-Fourier

* E-mail: Bruno.Lanson@obs.ujf-grenoble.fr

map was very diffuse, and specific sites for interlayer Na and H_2O could not be determined. This diffuseness was assumed to result from structural disorder (Post and Veblen 1990). Finally, the actual structural features responsible for the pronounced anisotropic peak broadening remained unclear. Anisotropic shapes of the coherent scattering domains (CSDs), and structural disorder along one direction, which was consistent with streaking observed in SAED patterns, were the two hypotheses invoked by Post and Veblen (1990).

In the present article, this anisotropic broadening is interpreted and, as a result, NaBi is shown to have a one layer triclinic sub-cell. By simulating the XRD pattern of NaBi with this sub-cell, new results concerning its sub-structure were obtained. In particular, interlayer sites for Na and H_2O have been re-determined and are now consistent with the model structure proposed by Drits et al. (1997), which relates the satellites observed on SAED patterns with a modulated distribution of interlayer Na and H_2O along the **b** axis. In addition, simulation of the NaBi XRD pattern provides direct evidence that negative layer charge and departure from the hexagonal layer symmetry originate from Mn^{3+} for Mn^{4+} substitution in octahedral layers.

Experimental methods

Sample NaBi1 was prepared following the procedure of Giovanoli et al. (1970a) as described by Drits et al. (1997); its structural formula is $Na^{1+}_{0.31}(Mn^{4+}_{0.69}Mn^{3+}_{0.31})O_2{\cdot}nH_2O$ (Silvester et al. 1997). One additional NaBi sample (NaBi2) was synthesized following the procedure of Feng et al. (1997). The initial NaBu suspension was prepared at room temperature using a $NaOH/Mn(NO_3)_2$ ratio of 3.3 and H_2O_2 as oxidizing agent. This suspension was then hydrothermally treated at 150 °C in a 1M NaOH solution for 24 hours to produce a NaBi suspension that was then filtered, washed, and dried at room temperature. Powder XRD patterns were obtained using Cu$K\alpha$ radiation with a Siemens D5000 powder diffractometer equipped with a Kevex Si(Li) solid detector. Intensities were measured at a 0.04° 2θ interval with a 30s counting time per step.

The XRD pattern of sample NaBi1 (Fig. 1) is almost identical to that reported by Post and Veblen (1990) but does not contain hausmannite. To a first approximation all major diffraction maxima can be indexed with a one-layer monoclinic sub-cell with a = 5.169 Å, b = 2.848 Å, c = 7.321 Å, and β = 103.2°. As noted by Post and Veblen (1990), there is strong anisotropic peak broadening, 11l reflections being much broader than 20l reflections for the same l value.

Thermal analysis was carried out with a Netzsch Simultan STA409EP micro-analyzer with a heating rate of 10 °C/min up to 1100 °C. Thermogravimetric analysis (TGA) and differential scanning calorimetry (DSC) were performed on ~20 mg samples to determine the weight loss due to adsorbed and interlayer water. Figure 2 shows that heating the NaBi1 sample induces two low-temperature weight losses that are likely related to the release of adsorbed (2.1%) and interlayer (7.1%) H_2O, respectively. To account for the loss of interlayer H_2O determined from TGA, the structural formula proposed by Silvester et al. (1997) for NaBi1 may be refined as $Na^{1+}_{0.31}(Mn^{4+}_{0.69}Mn^{3+}_{0.31})O_2{\cdot}0.40H_2O$.

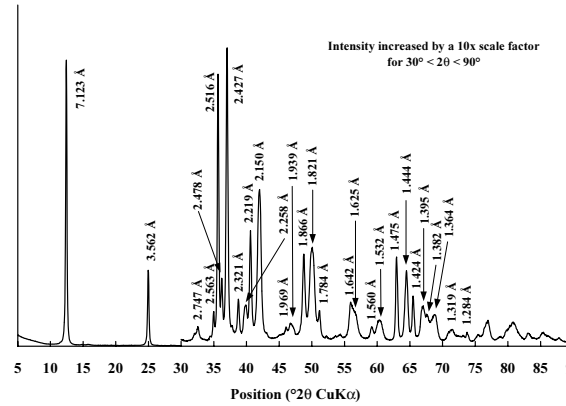

Figure 1. Experimental XRD pattern of synthetic NaBi1 sample.

Simulation of XRD patterns

To build up an initial structure model for NaBi, diffraction effects were calculated for crystal-chemically realistic structure models. The agreement between calculated and experimental XRD patterns was first improved using a trial-and-error procedure, as recommended by Drits and Tchoubar (1990) for defective structures. This approach was applied successfully to natural and synthetic one-layer hexagonal birnessites (Chukhrov et al. 1985; Manceau et al. 1997; Lanson et al. 2000), as well as to four-layer monoclinic Ca-exchanged birnessite (Drits et al. 1998). Details on the program used to calculate XRD patterns, as well as on the fitting procedure, are given by Drits et al. (1998). The background was assumed to be constant over the angular range considered (30–65 °2θ Cu$K\alpha$, 2.95–1.45 Å). The function used to describe the preferred orientation of particles is given by Drits and Tchoubar (1990).

Sub-cell parameters, atomic coordinates, and occupancies obtained from the trial-and-error approach were used to create an initial structural model for NaBi. Rietveld refinement of this model was subsequently carried out over a larger angular range using the computer program XND (Bérar and Baldinozzi 1998). To de-correlate instrumental broadening from defect broadening, PSF parameters and spectral distributions first were refined using a quartz reference, and then set constant during the refinement of the NaBi sub-structure. As in the previous calculations, the background was held constant over the considered angular range (34–90° 2θ Cu$K\alpha$, 2.95–1.09 Å). During initial cycles of the Rietveld refinement, only the scale factor was refined. In a second step, sub-cell parameters were refined prior to atomic coordinates and site occupancy factors. In the final stages of the refinement, preferred orientation was introduced using orientation dependent profiles, and calculating 00l lines as a separate phase having parameters identical to those used to calculate hkl reflections, but with different orientation-dependent profiles.

Results

Anisotropic broadening

Careful examination of the experimental XRD patterns (Figs. 1 and 3a) shows that the broadening of 11l reflections

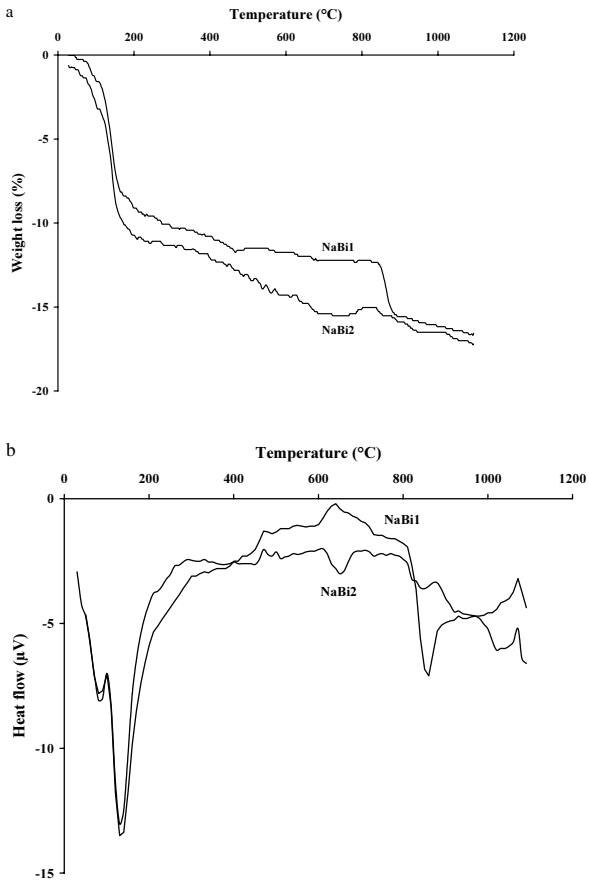

FIGURE 2. Experimental DTA-TG (**a**) and DSC (**b**) profiles obtained for synthetic NaBi1 and NaBi2 samples.

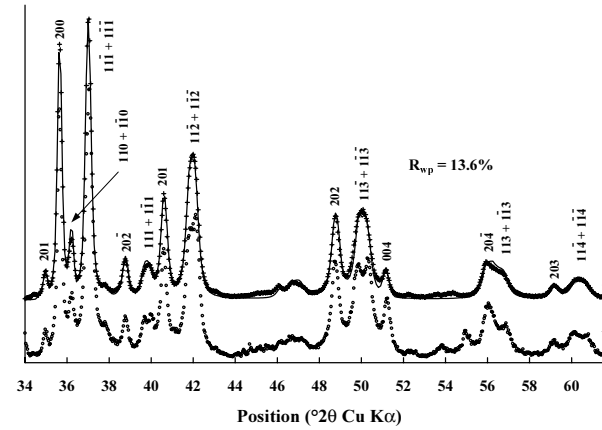

FIGURE 3. XRD patterns of synthetic NaBi1 (**a**) and NaBi2 (**b**) samples. The experimental pattern of NaBi1 sample (crosses), prepared according to the protocol of Giovanoli et al. (1970a), is compared with the optimal one obtained with the trial-and-error approach (solid line – only 20*l*, 11*l*, and $1\bar{1}l$ reflections are calculated). R_{wp} was calculated for the 34–62 °2θ range. a = 5.174 Å, b = 2.848 Å, c = 7.334 Å, α = 90.8°, β = 103.2°, and γ = 90°. Corresponding structural parameters are listed in the text except for the position of layer Mn (origin) and O (0.384, 0, 0.137) atoms and for the occupancy of interlayer sites (0.39 Na or H_2O in each site per unit cell).

increases with *l*, whereas 20*l* reflections are much sharper for the same *l* value, as described previously by Post and Veblen (1990). However, the intensity of 11*l* reflections does not decrease strongly as it would if this broadening were related only to structural disorder along the **b** axis. Because of the very similar breadths of 200 and 020 reflections, this broadening is unlikely to be associated with the anisotropic shape of the CSDs as suggested by Post and Veblen (1990). On the other hand, 11*l* reflections are clearly split for the NaBi2 sample (Fig. 3b – see especially $11\bar{2}$ and $1\bar{1}2$, $11\bar{3}$ and $1\bar{1}3$, and $11\bar{4}$ and $1\bar{1}4$ reflections), whereas the overall distribution of diffracted intensity is similar for the two samples. This split proves unambiguously the triclinic character of NaBi, and a triclinic sub-cell with parameters a = 5.174 Å, b = 2.848 Å, c = 7.334 Å, α = 90.5°, β = 103.2°, and γ = 90° indeed explains the observed selective broadening of 11*l* reflections. The sub-structure refinement was carried out on sample NaBi1 because sample NaBi2 contains a small manganite impurity, and because a model super-structure was available for this particular sample (Drits et al. 1997; Silvester et al. 1997). As a consequence, it was possible to interpret the structure model refined for NaBi1 in the light of available SAED and chemical data as the same sample was used.

Simulation of the NaBi XRD pattern

Trial-and-error approach. The similarity of the monoclinic (Post and Veblen 1990) and triclinic a, b, c, and α, β, γ sub-cell parameters suggests that the origin of the triclinicity of NaBi is a small layer displacement along the **b** axis. This shift lowers the space group *C*2/*m* (Post and Veblen 1990) to either $C\bar{1}$ or *C*1, probably without changing the layer symmetry (2/*m*). The present sub-structure refinement was performed using the centro-symmetric $C\bar{1}$ space group because no experimental argument in favor of a non-centro-symmetric sub-structure was found. At first, the XRD pattern of NaBi1 was simulated using positions and occupancies of layer and interlayer atomic sites refined by Post and Veblen (1990), taking into account the triclinic character of NaBi. In particular, Post and Veblen (1990) determined the presence of two interlayer sites, host to Na and H_2O, both of which were modeled with the scattering factor for oxygen. The predominant site (0.595, 0, 0.5) and the accessory site (0, 0, 0.5) had occupancy factors of 2.0 and 0.3 oxygen atoms per unit cell, respectively. However, the XRD pattern calculated for this model differs from the experimental one (Fig. 4a).

The trial-and-error approach was subsequently used to improve the initial structural model. Because of the modulated super-structures described by Drits et al. (1997) for sample NaBi1, and because of the diffuseness of the O2 site on the difference-Fourier map described by Post and Veblen (1990), splitting of the interlayer site was considered; the agreement between the calculated and experimental XRD patterns was significantly improved (Figs. 3 and 4b) by splitting the predominant interlayer position into four sites related by a center of symmetry (0.551, ±0.135, 0.500) and (0.449, ±0.135, 0.500). Even though at this stage structural sites for Na and H_2O can-

not be separated, the trial-and-error analysis clearly demonstrates that the predominant interlayer site is split (Figs. 4b and 4c).

Another conclusion obtained with the trial-and-error method is that NaBi1 contains very few stacking faults or other structural defects that alter its three-dimensional (3D) periodicity. The intensity and profiles of the measured reflections were reproduced assuming that cylinder-like CSDs have a 225 Å radius and contain an average of 20 birnessite layers, the amount of random stacking faults being only 3%. The NaBi sub-structure was further refined using the Rietveld technique.

The Rietveld approach. Atomic coordinates obtained with the trial-and-error approach in space group $C\bar{1}$ were transformed to space group $P\bar{1}$. Rietveld refinement of the sub-cell parameters gave values of a_P = 2.9513(4) Å, b_P = 2.9547(4) Å, c_P = 7.334(1) Å, α_P = 78.72(2)°, β_P = 101.79(1)°, and γ_P = 122.33(1)°. The refined positions and occupancies of structural sites for this sub-cell led to the fit shown in Figure 5. Final R_{WP} and R_B are respectively 10.7 and 6.2%. In spite of these high values, the refinement was stopped because the main discrepancies between experimental and calculated patterns arise from the presence of super-cell reflections in the XRD pattern of NaBi1. Furthermore, the discrepancy observed for the 200 reflection (Fig. 5) may be explained by the small amount of random stacking faults in this sample. Indeed, calculations performed using the trial-and-error approach show that the intensity calculated for this reflection strongly depends on the amount of such defects, and that the addition of random stacking faults (3–4%) to the refined model significantly improves the agreement between calculated and experimental distributions of intensities. As a consequence, no significant modification was expected for the sub-cell parameters. Refined structural parameters and selected inter-atomic distances of NaBi are found in Tables 1 and 2.

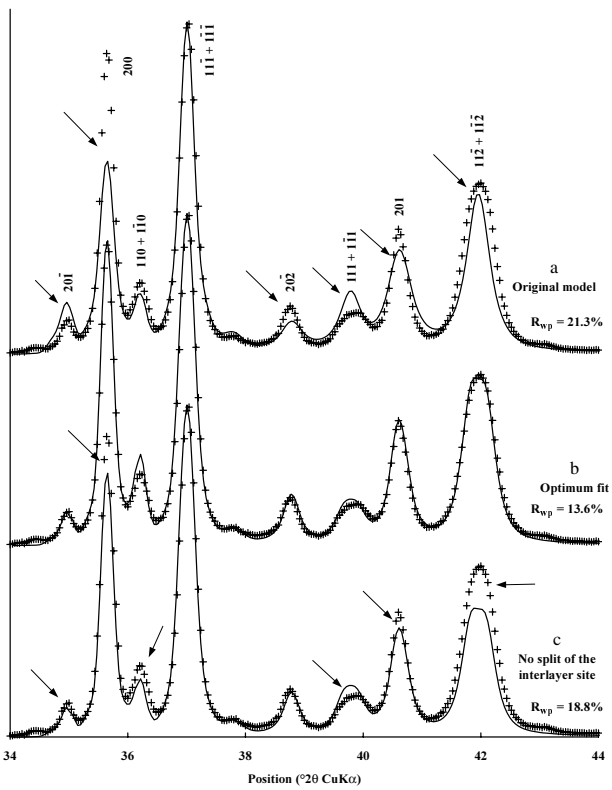

FIGURE 4. Influence of structural parameters on calculated XRD patterns as compared with the experimental NaBi1 pattern (crosses). (**a**) Calculation using the positions, (0.595, 0, 0.5) and (0, 0, 0.5), and the occupancy factors, 2.0 and 0.3, refined by Post and Veblen (1990). Other structural parameters as in the text and the caption of Figure 3. (**b**) Optimum fit obtained by splitting the predominant interlayer position into four sites related by a center of symmetry, (0.551, ±0.135, 0.500) and (0.449, ±0.135, 0.500), with 0.39 Na or H_2O per site. (**c**) Influence of the predominant interlayer position. Interlayer species are located in a unique non-split interlayer site (0.551, 0, 0.5) with 1.56 Na or H_2O per unit cell. All other structural parameters are constant. R_{wp} were calculated for restricted 34–62 °2θ range as in Figure 3.

Refinement of the layer Mn site occupancy factor for NaBi (range: 1.00 to 1.02) indicated that NaBi layers do not contain vacant octahedral sites. In addition, because the refined position of layer oxygen atoms (O_{layer}) is slightly off the long diagonal of the *P* sub-cell, the octahedral layer has no mirror plane, and its symmetry is lower than 2/*m*. Figure 6 shows the positions of four refined interlayer sites and the distances from these sites to the closest O_{layer} atoms. The analysis of these bond lengths allows determination of the nature of the interlayer species in these sites. For example, the two symmetrically related interlayer sites at 2.46 Å from the nearest O_{layer} are likely occupied by Na cations, whereas the other two symmetrically related sites, at ~2.70 Å from the nearest O_{layer} are likely occupied by H_2O (Fig. 6). Using this assumption, refined site occupancy factors for both Na (0.18 ± 0.02) and H_2O (0.27 ± 0.02) are similar to the values derived from the chemical formula (0.145 and 0.20, respectively) and support the hypothesized site allocation.

One may note that the same quality of fit may be obtained for a configuration of interlayer sites that, with respect to the first model, is almost symmetrically reflected by a plane passing through the $\mathbf{c}^*$ axis and the long diagonal of the *P* sub-cell. However, this alternative model was rejected because distances from each of the interlayer sites to the nearest O_{layer} atoms are significantly shorter than 2.5 Å, which is short for interlayer H_2O-O_{layer} bond lengths.

DISCUSSION

For clarity and to be consistent with previously published data, all structural features of NaBi are hereafter discussed in terms of the base-centered sub-cell with parameters *a* = 5.174

TABLE 1. Atomic positions, and site occupancy factors determined in the triclinic *P* sub-cell from the refined model shown in Figure 5

Atom	x	y	Z	Occ.
Mn_{layer}	0	0	0	0.5
O_{layer}	0.3886(26)	–0.3733(26)	0.1396(6)	1
Na_{Int}	0.628(11)	0.476(13)	0.481(3)	0.182(14)
H_2O_{Int}	0.290(8)	–0.819(15)	0.496(3)	0.272(16)

Notes: a_P = 2.9513(4) Å, b_P = 2.9547(4) Å, c_P = 7.334(1) Å, α_P = 78.72(2)°, β_P = 101.79(1)°, and γ_P = 122.33(1)°. Positions and site occupancy factors (Occ.) are given for space group P1bar. Un-refined isotropic B factors are 0.5 for Mn, 1 for O, and 2 for interlayer species. Layer and Int subscripts refer to the location of the atoms in the layer and in the interlayer, respectively.

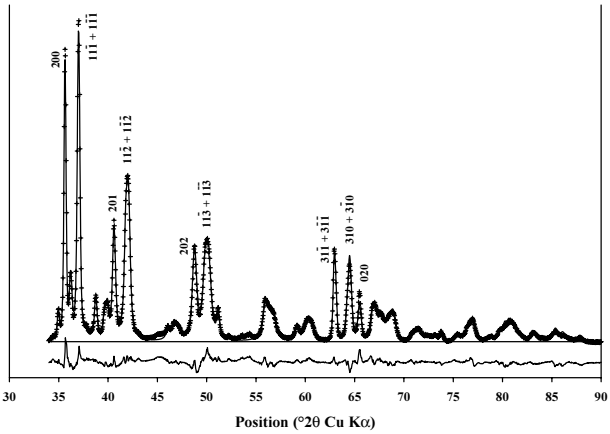

FIGURE 5. Final experimental (crosses), calculated, and difference powder XRD patterns for NaBi1 sample. The calculated background is indicated by the horizontal line.

TABLE 2. Selected bond lengths (Å) determined in the refined NaBi sub-structure

$Mn\text{-}O_1$	1.925(22) ×2	$Mn\text{-}O_1$	1.945(27) ×2	$Mn\text{-}O_1$	2.003(18) ×2
Mn-Mn	2.848 (36) ×2	Mn-Mn	2.951(0) ×2	Mn-Mn	2.955 (1) ×2
$O_1\text{-}O_1$	2.593(41)	$O_1\text{-}O'_1$	2.619(27)	$O_1\text{-}O'_1$	2.848(37) ×2
$O_1\text{-}O''_1$	2.620(18)	$O_1\text{-}O''_1$	2.951(13) ×2	$O'_1\text{-}O''_1$	2.955(12) ×2
$Na_i\text{-}O_i$	2.46(2)	$Na_i\text{-}O_{i\pm1}$	2.74(2)	$Na_i\text{-}H_2O_i$	2.61(6)
$Na_i\text{-}H_2O_{i\pm1}$	2.62(6)	$Na_i\text{-}H_2O_i$	2.64(6)	$Na_i\text{-}H_2O_{i\pm1}$	2.64(6)
$H_2O_i\text{-}O_i$	2.68(4)	$H_2O_i\text{-}O_{i\pm1}$	2.71(3)		

Å, b = 2.848 Å, c = 7.334 Å, α = 90.53°, β = 103.20°, and γ = 90.07°, which is equivalent to the refined primitive sub-cell with a_P = 2.951 Å, b_P = 2.955 Å, c_P = 7.334 Å, α_P = 78.72°, β_P = 101.79°, and γ_P = 122.33°.

Presence and azimutal orientation of Mn^{3+} octahedra in the layer

One of the most notable features of the NaBi layer is the strong elongation of individual octahedra along the **a** axis. Within an MnO_6 octahedron, the two Mn-O distances oriented in the $\mathbf{ac}^*$ plane are much longer (2.003 Å) than the other four Mn-O distances (1.945 and 1.925 Å; Table 2). This elongation originates from the displacement along the **a** axis of O_{layer} atoms lowering the ideal symmetry of the octahedron. Additionally, this elongation is responsible for the departure from hexagonal symmetry of the layer ($a/b = 1.817 = \sqrt{3.30}$). This distortion likely results from the presence of a significant amount of Mn^{3+} cations in NaBi; two Mn^{3+}-O distances in Mn^{3+} octahedra are commonly much longer than the other four because of the Jahn-Teller effect. In crednerite, for example, Mn^{3+} octahedra contain two 2.260 Å and four 1.929 Å Mn^{3+}-O bond lengths, with an average <Mn-O> distance of 2.04 Å (Töpfer et al. 1995). Similar distortions of Mn^{3+} octahedra and <Mn^{3+}-O> have been reported by Shannon et al. (1975) for α-MnOOH (2.041 Å, Glasser and Ingram 1968), γ-MnOOH (2.037 Å, Dachs 1963), and $\alpha\text{-}Mn_2O_3$ (2.039–2.045 Å - Norrestam 1967).

If one assumes that <Mn-O> is a statistically weighted sum of the mean Mn^{3+}-O distance determined for crednerite and for Mn oxy-hydroxides (~2.04 Å), and of the Mn^{4+}-O distance, determined for $\lambda\text{-}MnO_2$ (1.912 Å, Thackeray et al. 1993), the mean Mn-O distance for the 0.69:0.31 cation composition of NaBi1 should be 1.952 Å. This value is close to the observed one (1.958 Å). For the same average layer cation composition ($Mn^{4+}_{0.69}Mn^{3+}_{0.31}$), the long Mn-O distance calculated as the weighted sum of long Mn-O distances determined for Mn^{4+} and Mn^{3+} octahedra for $\lambda\text{-}MnO_2$ (1.912 Å) and crednerite (2.26 Å), respectively, equals 2.020 Å and is similar to the experimentally determined value (2.003 Å). As a consequence, the origin of the negative layer charge is undoubtedly the presence of Mn^{3+} cations, rather than the existence of vacant layer sites. Furthermore, the distribution of Mn-O distances indicates that all Mn^{3+} octahedra have the same azimutal orientation, with their long Mn-O distance in the $\mathbf{ac}^*$ plane. This unique azimutal orientation is responsible for the departure from the hexagonal layer symmetry.

Structure of the interlayer region

As compared with the model proposed by Post and Veblen (1990), the main difference in our refined model of the NaBi interlayer region is the determination of specific sites for Na and H_2O. Post and Veblen (1990) did not determine the respective positions of these interlayer species because the maximum observed in their difference-Fourier map was very diffuse, and because of the very similar scattering powers of these two species. To account for this diffuseness, these authors invoked positional disorder in the distribution of interlayer species possibly occupying "different sites within a unit-cell and a range of positions in different unit cells." The results of our refinement support this hypothesis, as within the sub-cell Na and H_2O occupy different sites related by a center of symmetry (Figs. 6, 7, and 8). Such a split of Na and H_2O sites is likely responsible for the diffuse character of the electron density described by Post and Veblen (1990). The two Na sites are shifted along the $\mathbf{c}^*$ axis, one toward the lower layer (Na_1) and the other toward the upper layer (Na_2; Fig. 8), leading to typical $Na_i\text{-}O_i$ distances (2.46 Å).

The existence of two distinct H_2O sites is favored by the equal opportunity for the formation of strong hydrogen bonds between interlayer H_2O and layer oxygen atoms offered by each of these positions (Fig. 7). According to our refinement, the two H_2O sites differ from each other by their z-coordinate; one site is shifted toward the lower octahedral layer [$z = 0.495 - (H_2O)_1$] whereas the other is shifted toward the upper layer [$z = 0.505 - (H_2O)_2$]. If the nearest oxygen atoms of adjacent lower and upper layers are respectively labeled O_1 and O_2, bond lengths $(H_2O)_1\text{-}O_1$, $(H_2O)_2\text{-}O_2$ (2.69 Å), and $(H_2O)_2\text{-}O_1$ and $(H_2O)_1\text{-}O_2$ (2.71 Å) are typical for the formation of H-bonds (Fig. 7). Furthermore, the 145° angle between O_1, O_2, and H_2O_i (i = 1, 2; Fig. 7) is also suitable for the formation of strong H-bonds that are responsible for most of the cohesion between layers.

Origin of the super-cell and modulated structures

The results of our refinement on NaBi1 confirm unambiguously the assumption of Post and Veblen (1990), Manceau et al. (1992), and Drits et al. (1997) that super-cell reflections and satellites observed in the SAED patterns of NaBi microcrystals result from a regular distribution of interlayer species

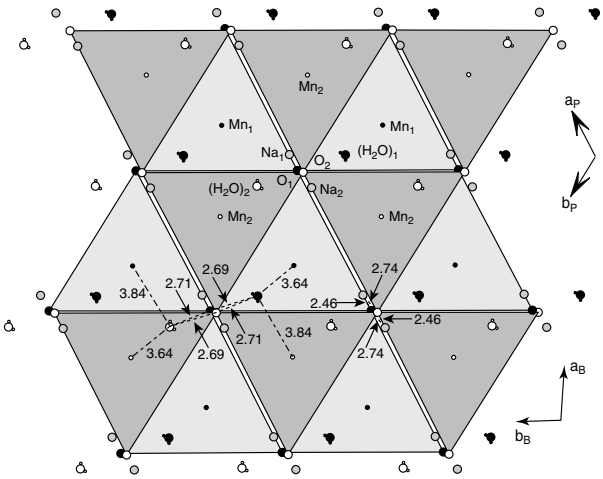

FIGURE 6. Schematic location of interlayer Na and H_2O sites with respect to layer O and Mn atoms in projection on the **a-b** plane. Inter-atomic distances are given in Å. Positions and distances are listed in Tables 1 and 2. Layer O and Mn atoms are shown as large and small circles. Atoms of the lower (subscript 1) and upper (subscript 2) layers are shown as solid and open circles, respectively. Interlayer species closer to the lower and upper layer are labeled with subscripts 1 and 2, respectively. $(H_2O)_1$ and $(H_2O)_2$ molecules are shown as solid and open symbols, respectively, whereas the two Na cations are shown as shaded circles. *P* and *B* subscripts refer to the primitive and base-centered sub-cell parameters, respectively.

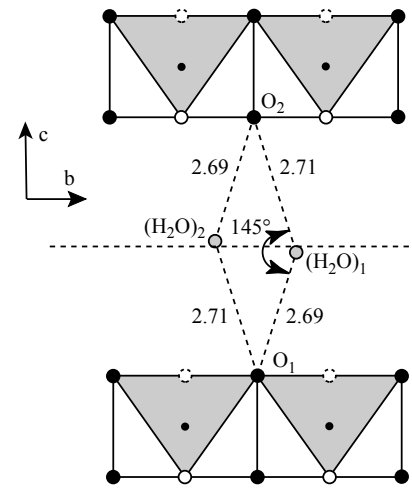

FIGURE 7. Schematic location of interlayer H_2O sites with respect to layer O atoms in projection along the **a** axis. Inter-atomic distances are given in Å. Positions and distances are listed in Tables 1 and 2. Layer O and Mn atoms are shown as large and small circles. Subscripts as in Figure 6. H_2O molecules are shown as shaded circles.

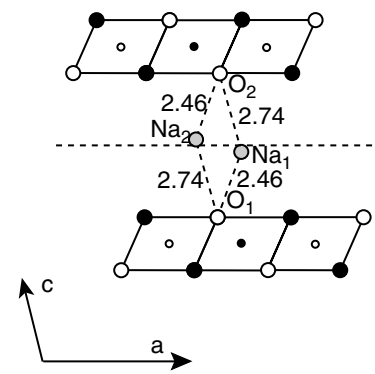

FIGURE 8. Schematic location of interlayer Na sites with respect to layer O atoms in projection along the **b** axis. Inter-atomic distances are given in Å. Positions and distances are listed in Tables 1 and 2. Subscripts as in Figure 6. Layer O and Mn atoms are shown as large and small circles. Na cations are shown as shaded circles. Open circles indicate atoms at $y = 0$, and solid symbols indicate atoms at $y = \pm 1/2$.

rather than vacancies in the octahedral layer.

For NaBi micro-crystals, two types of SAED patterns have been reported (Drits et al. 1997). The distribution of super-cell reflections in NaBi type I corresponds to a base-centered layer super-cell with $A = 3a = 15.52$ Å, $B = b = 2.848$ Å, and $\gamma = 90°$. To account for these super-cell reflections, Drits et al. (1997) proposed the arrangement of interlayer Na cations shown in Figure 9a. In addition, any sub- and super-cell reflection is surrounded by satellites at $\pm b^*/6$ along the $[01]^*$ direction. According to Drits et al. (1997) these satellites arise from a periodic variation of distances between planes parallel to (010) containing interlayer species (Fig. 10). The distribution of super-cell reflections reported for NaBi type II corresponds to a base-centered super-cell with $A = 3a = 15.52$ Å, $B = 3b = 8.55$ Å, and $\gamma = 90°$. A possible distribution of Na within the interlayer super-cell is shown in Figure 9b. As discussed by Drits et al. (1997), the (0, 0) and the (0.5, 0.5) sites should be fully occupied whereas other sites are occupied by Na with a lower probability to maintain the base-centered character of the interlayer Na distribution (Fig. 9b).

In both NaBi varieties, the super-periodicity $A = 3a$ arises from the ordered distribution of Mn^{3+}-rich rows parallel to [010], separated from each other along [100] by two Mn^{4+} rows (Drits et al. 1997). Along with sub- and super-cell reflections, SAED patterns of NaBi type II contain two types of satellites: (1) the first type is similar to those observed for NaBi type I, and (2) the second type is elongated along $[11]^*$ and $[1\bar{1}]^*$. Satellites elongated along $[1\bar{1}]^*$ are located in the middle of two nearest point reflections located along $[11]^*$. A possible arrangement of interlayer species that accounts for the main diffraction features of NaBi type II is shown in Figure 11. A periodic displacement of Na and H_2O along the **b** axis with $B_s = 6b$ accounts for the origin of the satellites of the first type. A periodic modulation along [13] and $[\bar{1}3]$ of Na and H_2O species located along (110) and $(1\bar{1}0)$, respectively, gives rise to the satellites of the second type. As can be seen in Figure 11, waves parallel to (110) located in two neighboring rhomb-shaped unit cells (I and II) do not scatter X-rays strictly in phase because of opposite displacements of Na and H_2O along the **b** axis. This phase difference is likely responsible for the elongation of the satellites (Drits et al. 1997).

Results from the present refinement may be combined with

the above interpretation of SAED patterns to propose consistent 2D distributions of interlayer Na and H_2O responsible for the presence of super-cell reflections and satellites for both NaBi type I and II crystals.

NaBi type II. In agreement with SAED data, Na cations should be distributed with a 3*b* period along the **b** axis of a super-cell with $A = 3a$, $B = 3b$, $\gamma = 90°$ (Fig. 9b). To comply with the two positions determined for Na, these cations are likely shifted along the **b** axis alternately toward the upper and lower layer surfaces to provide homogeneous compensation of the negative layer charge. As a result, Na cations form an Na_1-Na_2-Na_1… sequence inducing a 6*b* period along the **b** axis consistent with the satellite periodicity. In addition to O_{layer} atoms, Na cations are likely coordinated by H_2O molecules at 2.60–2.65 Å, and H_2O molecules coordinating Na_i cations are located in the H_2O_i sites. The combination of the above conditions leads to the 2D distribution of interlayer Na and H_2O shown in Figure 12.

This distribution presents several remarkable features. First, interlayer cohesion is insured by a set of chains, elongated along the **a** axis, in which Na and H_2O are distributed in an Na_i-$(H_2O)_i$-Na_i-$(H_2O)_i$… sequence ($i = 1, 2$). As a consequence, each Na is tetrahedrally coordinated by two O_{layer} atoms at 2.46 and 2.74 Å and by two H_2O molecules at 2.61 and 2.64 Å. Similarly, in these chains each H_2O is bound to two O_{layer} atoms (2.69–2.71 Å) and to two Na cations (2.61–2.64 Å). On Figure 12, one may note that successive chains are not linked to each other by inter-chain interlayer species. Second, the distance between successive chains changes periodically along the **b** axis with a 6*b* super-periodicity because the displacements of Na cations

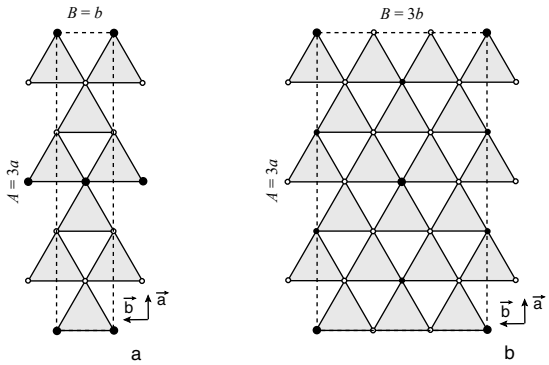

FIGURE 9. Super-cells for NaBi types I and II with $A = 3a$ and $B = b$ (**a**), and $A = 3a$ and $B = 3b$ (**b**). In the two super-cells, solid and open circles correspond to interlayer Na and H_2O positions, respectively. In the first super-cell (**a**), the occupancy factor for Na sites is 0.5, whereas in the second super-cell (**b**), the (0,0) and the (0.5, 0.5) positions (large solid circles) have a higher occupancy than the other positions (small solid circles, modified from Drits et al. 1997).

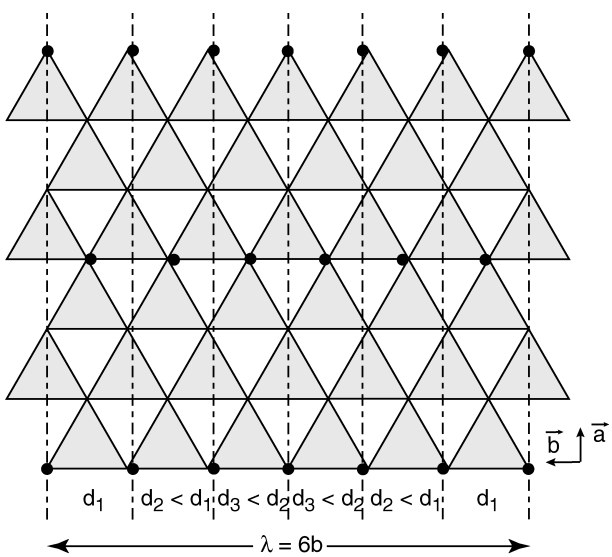

FIGURE 10. Idealized super-structure model for NaBi interlayers of type I. Gray triangles correspond to the upper surface of the lower layer. Solid circles represent Na-rich interlayer sites. The thick vertical lines with variable distances correspond to (010) planes (irregular dashed lines), which contain Na sites (modified from Drits et al. 1997).

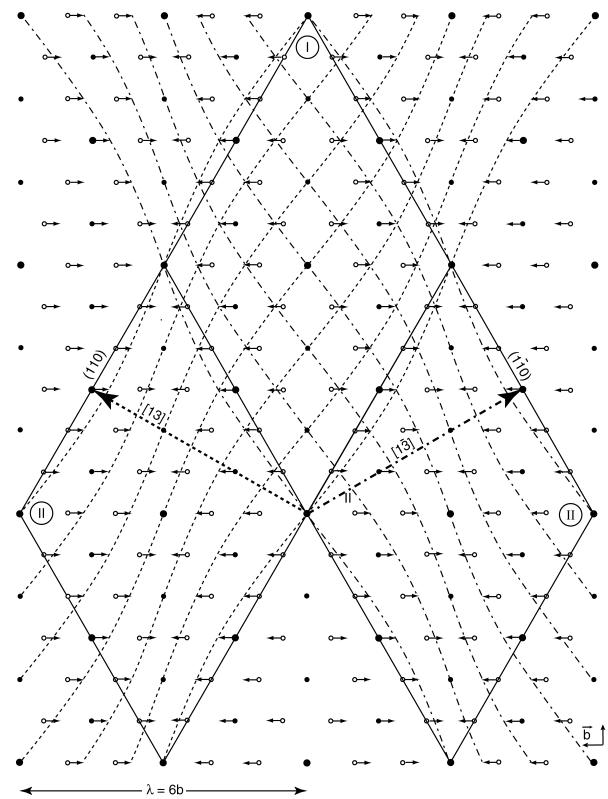

FIGURE 11. Idealized super-structure model for NaBi interlayers of type II. Large and small solid circles represent Na sites with different degrees of occupancy. Small open circles correspond to H_2O sites. Arrows attached to circles indicate the periodic displacement of interlayer species along the **b** axis with a $B_S = 6b$ period. Rhomb-shaped unit cells I and II have the same sizes and shapes but differ slightly in the arrangement of Na and H_2O sites. Variations of $d_{(010)}$ and $d_{(110)}$ are equal to 6*b* and 6*a*, respectively (modified from Drits et al. 1997).

along the **b** axis induce the same periodicity in the distribution of associated H_2O. As shown on Figure 13a, the shift of interlayer Na along the **c** axis and in the **ab** plane likely results from the Mn^{3+}-Mn^{3+}-Mn^{3+}-Mn^{3+}-Mn^{2+}-Mn^{4+}… distribution of heterovalent Mn_{layer} in Mn^{3+}-rich rows described by Drits et al. (1997), interlayer Na being shifted toward Mn^{2+} cations. To account for the observed $B = 3b$ super-cell periodicity, the respective positions of heterovalent Mn_{layer} sequences in adjacent layers must be considered. If Mn^{3+}-rich rows from adjacent layers are shifted by –**a**/3 with respect to each other, sequences of heterovalent Mn_{layer} cations in these Mn^{3+}-rich rows should be shifted along the **b** axis to induce the observed $B = 3b$ super-cell periodicity, as shown on Figure 13b. As a result, Na_1 and Na_2 cations are shifted in opposite directions along the **c** axis and in the **ab** plane leading to the modulated distance between successive chains of interlayer species, which in turn is responsible for satellites of the first type observed in SAED patterns of NaBi type II crystals.

The third feature of the interlayer species distribution shown on Figure 12 is the fluctuation, along [13] and [1$\bar{3}$], of interlayer Na and H_2O atomic positions. As an illustration, a rhomb-shaped unit cell with $2(\mathbf{A} + \mathbf{B})$ and $2(\mathbf{B} - \mathbf{A})$, or $12\mathbf{a}_P$ and $12\mathbf{b}_P$, may be chosen (A, B, a_P, and b_P are parameters of the base-centered super-cell and of the primitive sub-cell, respectively; Fig. 14). One may note that interlayer Na and H_2O (not shown) are distributed periodically as waves parallel to (110), or b_P. The amplitude of these waves varies along [13] with a $8d_{(310)}$ (or $12a_p$) period. Drits and Kashaev (1969) showed that a periodic displacement of atoms along the **a** axis with a $\lambda = nb$ period along the **b** axis induces, in reciprocal space, satellites that are located along the $\mathbf{b}^*$ axis and separated from the main nodes by b^*/n. Similarly, the periodic displacement of interlayer species (Na and H_2O) along [13] with a $8d_{(310)}$ (or $12a_p$) period along [11] should induce satellites distributed along [1$\bar{1}$]* and separated from super-cell reflections by $a_p^*/12$ (or $B^*/4\sin\gamma$). Similar displacements of interlayer species along [1$\bar{3}$] (not shown) induce additional satellites located along [11]* at the same distance from super-cell reflections as the previous group of satellites. Such satellite distribution has been described as satellites of the second type in SAED patterns of NaBi crystals type II (Drits et al. 1997).

NaBi type I. As mentioned, this variety has a layer super-cell with $A = 3a = 15.52$ Å, $B = b$, $\gamma = 90°$ (Fig. 9a), and the presence of satellites indicates the existence of a modulated super-cell with a $6b$ period. As a consequence, the 2D distribution of interlayer Na and H_2O in NaBi type I crystals should satisfy several conditions. First, Na cations should form rows parallel to the **b** axis and separated from each other by $A/2$ along the **a** axis. In addition, successive Na should be separated from each other by distances of $2b$ along the **b** axis to

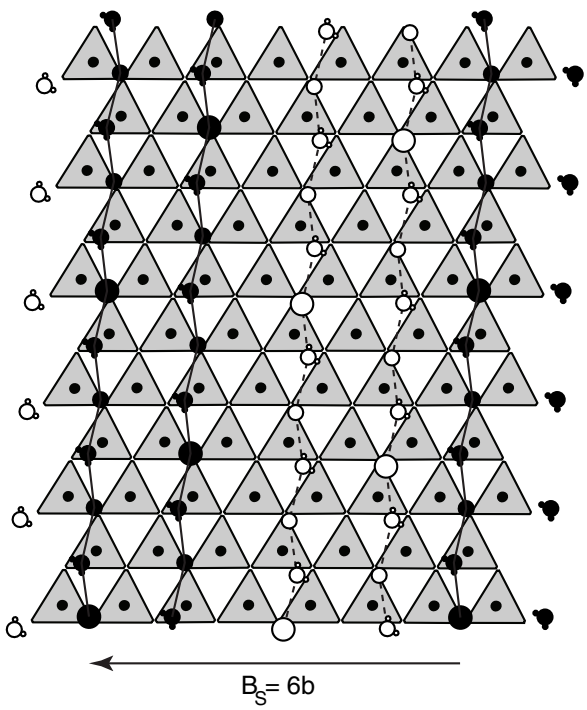

FIGURE 12. Schematic distribution of interlayer species in projection on the **a-b** plane for NaBi type II crystals. All symbols as in Figure 6, except for Na_1 and Na_2 cations, which are shown as solid and open large circles, respectively. Na sites with a higher occupancy are shown as enlarged circles. Na_i-$(H_2O)_i$-Na_i-$(H_2O)_i$… chains parallel to the **a** axis with i = 1, 2 are shown as solid and dashed lines, respectively.

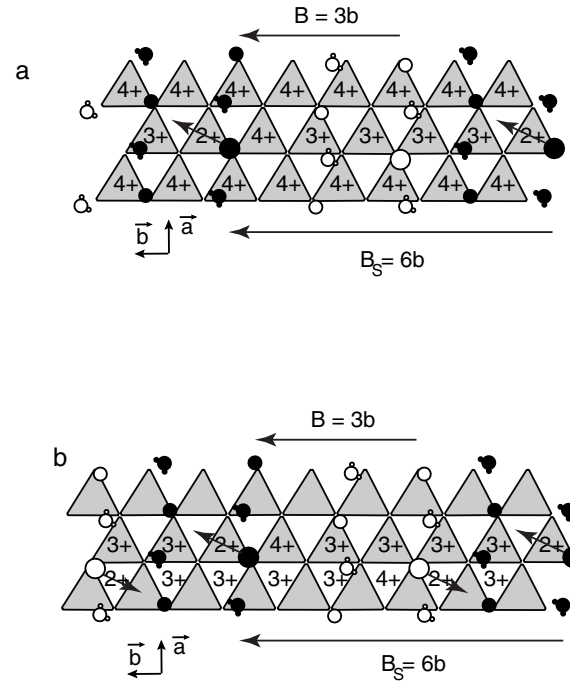

FIGURE 13. Schematic distribution of interlayer species in projection on the **a-b** plane for NaBi type II crystals. All symbols as in Figure 12. Heterovalent Mn layer cations are shown as 2+, 3+, and 4+. (**a**) Distribution of heterovalent Mn cations in the lower layer. In Mn^{3+}-rich rows, Mn cations are distributed as Mn^{3+}-Mn^{3+}-Mn^{3+}-Mn^{3+}-Mn^{2+}-Mn^{4+}… (Drits et al. 1997). The shift of interlayer Na induced by the presence of Mn^{2+} is shown by the arrow. (**b**) Distribution of heterovalent Mn cations in the Mn^{3+}-rich rows of two adjacent layers. Mn_{layer} from the upper layer are shifted by –**a**/3 with respect to those of the lower layer. Shift of interlayer Na toward Mn^{2+} cations is indicated by arrows.

avoid Na-Na pairs. Second, to generate the modulated structure responsible for the satellites, Na cations should be specifically distributed along these rows with a 6*b* period, as in Na_1-Na_1-Na_2-Na_1…, and Na_2-Na_2-Na_1-Na_2… sequences. In addition, one may assume that predominant Na-O_{layer} distances are 2.61–2.64 Å, inducing Na_i-O_i-O_i-Na_i… (i = 1, 2) sequences of interlayer species along the **a** axis. Third, to induce an average *b* period for the base-centered super-cell, the rows separated by *A*, as well as rows separated by *A*/2, should be shifted at random with respect to each other by ±*b*.

A 2D distribution of interlayer species in NaBi type I satisfying these conditions is shown in Figure 15. As for NaBi type II, each Na has tetrahedral coordination with the same bond lengths and each H_2O is bound to the two nearest O_{layer} atoms and to two Na cations. Figure 15a shows that interlayer Na and H_2O form chains elongated along the **a** axis (solid lines). The distance between these chains along the **b** axis changes with a $\lambda = 6b$ period, accounting for the satellites observed in SAED patterns of NaBi type I crystals (Drits et al. 1997). An alternative origin for these satellites (Drits and Kashaev 1969) is a periodic displacement of interlayer species along the **a** axis with a 6*b* period along the **b** axis (Fig. 15a). In these chains, there are two equally probable configurations for H_2O-H_2O pairs. As a consequence, propagation of these chains along the **a** axis may be random (Fig. 15b; dashed lines), inducing the average $B = b$ periodicity.

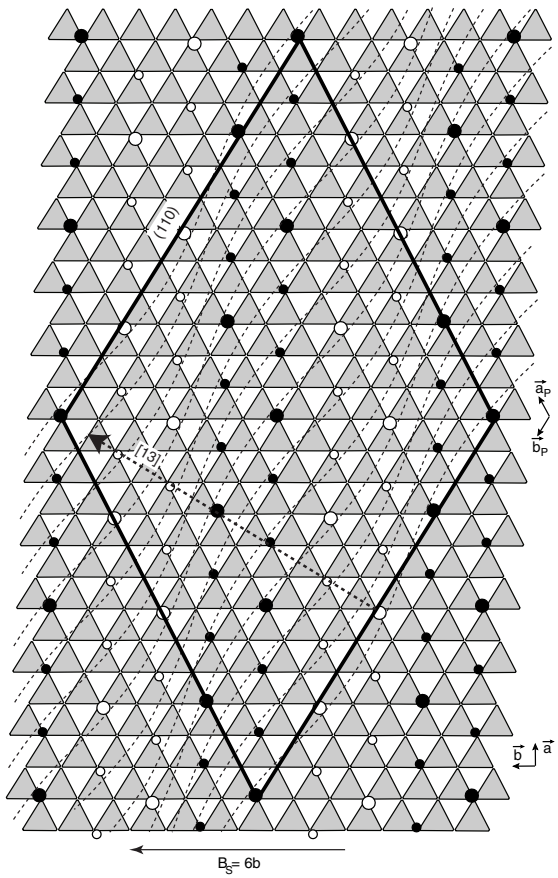

FIGURE 14. Schematic distribution of interlayer species in projection on the **a-b** plane for NaBi type II crystals. All symbols as in Figure 12. Dashed lines outline the periodic displacement of interlayer Na parallel to (110), whose amplitude varies along [13] with a $8d_{(310)}$ (or $12a_p$) period. The thick solid line outlines the rhomb-shaped unit-cell with $2(A + B)$ and $2(B - A)$, or 12 a_P and 12 b_P.

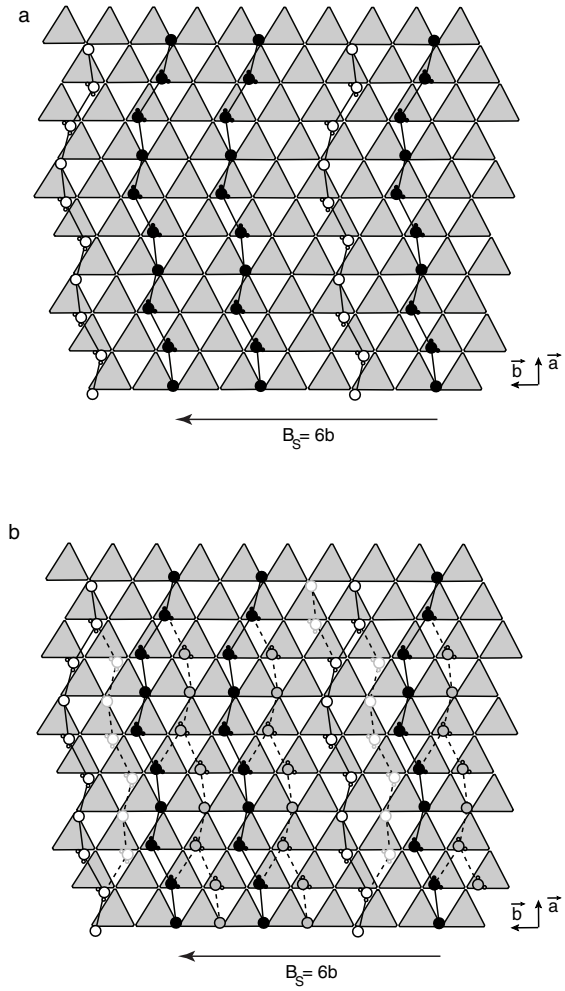

FIGURE 15. Schematic distribution of interlayer species in projection on the **ab** plane for NaBi type I crystals. All symbols as in Figure 12. One possible 2D distribution of interlayer species is shown in Figure 15a, whereas Figure 15b shows an alternative distribution induced by different geometric configurations of H_2O-H_2O pairs.

ACKNOWLEDGMENTS

The authors thank Ewen Silvester for supplying the $NaBi_1$ birnessite sample, Pr. Alain Plançon and Jean-François Bérar for their programs. V.A.D. is grateful to the Russian Science Foundation for financial support. B.L. acknowledges financial support from INSU/Géomatériaux and CNRS/PICS709 programs. Michel Garais (University of Poitiers) is thanked for the thermal analysis of NaBi samples. Constructive remarks and comments by AE David Bish and two anonymous reviewers helped to improve the original manuscript.

REFERENCES CITED

Balistrieri, L.S. and Murray, J.W. (1982) The surface chemistry of δ–MnO_2 in major ion seawater. Geochimica et Cosmochimica Acta, 46, 1041–1052.

Bérar, J.F. and Baldinozzi, G. (1998) Xnd code: from X-ray laboratory data to

incommensurately modulated phases. Rietveld modeling of complex materials. CPD Newsletter, 20, 3–5.
Bidoglio, G., Gibson, P.N., O'Gorman, M., and Roberts, K.J. (1993) X-ray absorption spectroscopy investigation of surface redox transformations of thallium and chromium on colloidal mineral oxides. Geochimica et Cosmochimica Acta, 57, 2389–2394.
Bricker, O. (1965) Some stability relations in the system Mn-O_2-H_2O at 25° and one atmosphere total pressure. American Mineralogist, 50, 1296–1354.
Burns, R.G. and Burns, V.M. (1976) Mineralogy of ferromanganese nodules. In G.P. Glasby, Ed., Marine manganese deposits, p. 185–248. Elsevier, Amsterdam.
Chen, R., Zavalij, P., and Whittingham, M.S. (1996) Hydrothermal synthesis and characterization of $K_xMnO_2.yH_2O$. Chemistry of Materials, 8, 1275–1280.
Chukhrov, F.V. and Gorshkov, A.I. (1981) Iron and manganese oxide minerals in soils. Transactions of the Royal Society of Edinburgh, 72, 195–200.
Chukhrov, F.V., Gorschkov, A.I., Rudnitskaya, E.S., and Sivtsov, A.V. (1978) Birnessite characterization. Investiya Akademie Nauk, SSSR, Seriya Geologicheskaya, 9, 67–76.
Chukhrov, F.V., Sakharov, B.A., Gorshkov, A.I., Drits, V.A., and Dikov, Y.P. (1985) Crystal structure of birnessite from the Pacific ocean. International Geology Review, 27, 1082–1088.
Chukhrov, F.V., Gorshkov, A.I., and Drits, V.A. (1989) Supergenic manganese hydrous oxides. 208 p. Nauka, Moscow.
Cornell, R.M. and Giovanoli, R. (1988) Transformation of hausmannite into birnessite in alkaline media. Clays & Clay Minerals, 36, 249–257.
Dachs, H. (1963) Neutronen- und Röntgenuntersuchungen am Manganit, MnOOH. Zeitschrift für Kristallographie, 118, 303–326.
Drits, V.A. and Kashaev, A.A. (1969) The origin of satellites in the reciprocal lattice of cymrite. Soviet Physics Crystallography, 13, 700–704.
Drits, V.A. and Tchoubar, C. (1990) X-ray diffraction by disordered lamellar structures: Theory and applications to microdivided silicates and carbons. 371 p. Springer-Verlag, Berlin.
Drits, V.A., Petrova, V., and Gorshkov, A.I. (1985) Manganese minerals of Fe-Mn nodules from the sediments of the central part of Pacific Ocean and their post-sedimentation transformation. Lithology and Raw Materials, 3, 17–39.
Drits, V.A., Silvester, E.J., Gorshkov, A.I., and Manceau, A. (1997) The structure of monoclinic Na-rich birnessite and hexagonal birnessite. Part 1. Results from X-ray diffraction and selected area electron diffraction. American Mineralogist, 82, 946–961.
Drits, V.A., Lanson, B., Gorskhov, A.I., and Manceau, A. (1998) Sub- and superstructure of four-layer Ca-exchanged birnessite. American Mineralogist, 83, 97–118.
Feng, Q., Sun, E.H., Yanagisawa, K., and Yamasaki, N. (1997) Synthesis of birnessite-type sodium manganese oxides by solution reaction and hydrothermal methods. Journal of the Ceramic Society of Japan, 105, 564–568.
Giovanoli, R., Stähli, E., and Feitknecht, W. (1970a) Über Oxidhydroxide des vierwertigen Mangans mit Schichtengitter. 1. Mitteilung: Natriummangan(II,III)manganat(IV). Helvetica Chimica Acta, 53, 209–220.
——— (1970b) Über Oxidhydroxide des vierwertigen Mangans mit Schichtengitter. 2. Mitteilung: Mangan(III)-manganat(IV). Helvetica Chimica Acta, 53, 453–464.
Glasser, L.S.D. and Ingram, L. (1968) Refinement of the crystal structure of Groutite, α-MnOOH. Acta Crystallographica, B24, 1233–1236.
Glover, E.D. (1977) Characterization of a marine birnessite. American Mineralogist, 62, 278–285.
Golden, D.C., Dixon, J.B., and Chen, C.C. (1986) Ion exchange, thermal transformations, and oxidizing properties of birnessite. Clays & Clay Minerals, 34, 511–520.
Healy, T.W., Herring, A.P., and Fuerstenau, D.W. (1966) The effect of crystal structure on the surface properties of a series of manganese dioxides. Journal of Colloid and Interface Science, 21, 435–444.
Lanson, B., Drits, V.A., Silvester, E.J., and Manceau, A. (2000) Structure of H-exchanged hexagonal birnessite and its mechanism of formation from Na-rich monoclinic buserite at low pH. American Mineralogist, 85, 826–838.
Le Goff, P., Baffier, N., Bach, S., and Pereira-Ramos, J.-P. (1996) Synthesis, ion exchange and electrochemical properties of lamellar phyllomanganates of the birnessite group. Materials Research Bulletin, 31, 63–75.
Manceau, A. and Charlet, L. (1992) X-ray absorption spectroscopic study of the sorption of Cr(III) at the oxide-water interface. Journal of Colloid and Interface Science, 148, 425–442.
Manceau, A., Gorshkov, A.I., and Drits, V.A. (1992) Structural Chemistry of Mn, Fe, Co, and Ni in Mn hydrous oxides. II. Information from EXAFS spectroscopy, electron and X-ray diffraction. American Mineralogist, 77, 1144–1157.
Manceau, A., Drits, V.A., Silvester, E.J., Bartoli, C., and Lanson, B. (1997) Structural mechanism of Co^{2+} oxidation by the phyllomanganate buserite. American Mineralogist, 82, 1150–1175.
Murray, J.W. (1974) The surface chemistry of hydrous manganese dioxide. Journal of Colloid and Interface Science, 46, 357–371.
Norrestam, R. (1967) α-Manganese (III) oxide–A C-type sesquioxide of orthorhombic symmetry. Acta Chemica Scandinavica, 21, 2871–2884.
Paterson, E., Swaffield, R., and Clark, L. (1994) The influence of structure on Ba and K uptake by a synthetic phyllomangante. Clay Minerals, 29, 215–222.
Post, J.E. and Appleman, D.E. (1988) Chalcophanite, $ZnMn_3O_7$-$3H_2O$: New crystal-structure determinations. American Mineralogist, 73, 1401–1404.
Post, J.E. and Veblen, D.R. (1990) Crystal structure determinations of synthetic sodium, magnesium, and potassium birnessite using TEM and the Rietveld method. American Mineralogist, 75, 477–489.
Shannon, R.D., Gumeman, P.S., and Chenavas, J. (1975) Effect of octahedral distortion on mean Mn^{3+}-O distances. American Mineralogist, 60, 714–716.
Silvester, E.J., Manceau, A., and Drits, V.A. (1997) The structure of monoclinic Na-rich birnessite and hexagonal birnessite. Part 2. Results from Chemical Studies and EXAFS Spectroscopy. American Mineralogist, 82, 962–978.
Stälhi, E. (1968) Ueber Manganate (IV) mit Schichtenstruktur. Anorganisch-Chemisches Institut, p. 198, Bern.
Stone, A.T. (1987) Reductive dissolution of manganese (III/IV) oxides by substituted phenols. Environmental Science & Technology, 21, 979–993.
Stone, A.T. and Morgan, J.J. (1984) Reductive dissolution of manganese (III) and manganese (IV) oxides by organics. Environmental Science & Technology, 18, 617–624.
Stone, A.T., Godtfredsen, K.L., and Deng, B. (1994) Sources and reactivity of reductant encountered in aquatic environments. In G. Bidoglio, and W. Stumm, Eds. Chemistry of aquatic systems: Local and global perspectives, p. 337–374. ECSC, EEC, EAEC, Brussels.
Strobel, P., Charenton, J.-C., and Lenglet, M. (1987) Structural chemistry of phyllomanganates: Experimental evidence and structural models. Revue de Chimie Minérale, 24, 199–220.
Taylor, R.M., McKenzie, R.M., and Norrish, K. (1964) The mineralogy and chemistry of manganese in some Australian soils. Australian Journal of Soil Research, 2, 235–248.
Thackeray, M.M., de Kock, A., and David, W.I.F. (1993) Synthesis and structural characterisation of defect spinels in the lithium-manganese-oxide system. Materials Research Bulletin, 28, 1041–1049.
Töpfer, J., Trari, M., Gravereau, P., Chaminade, J.P., and Doumerc, J.P. (1995) Crystal growth and reinvestigation of the crystal structure of crednerite, $CuMnO_2$. Zeitschrift für Kristallographie, 210, 184–187.
Tu, S., Racz, G.J., and Goh, T.B. (1994) Transformations of synthetic birnessite as affected by pH and manganese concentration. Clays & Clay Minerals, 42, 321–330.
Usui, A. and Mita, N. (1995) Geochemistry and mineralogy of a modern buserite deposit from a hot spring in Hokkaido, Japan. Clays & Clay Minerals, 43, 116–127.
Xyla, A.G., Sulzberger, B., Luther, G.W., Hering, J.G., Van Capellen, P., and Stumm, W. (1992) Reductive dissolution of manganese(III,IV) (hydr)oxides by oxalate: The effect of pH and light. Langmuir, 8, 95–103.

MANUSCRIPT RECEIVED JULY 24, 2001
MANUSCRIPT ACCEPTED JUNE 2, 2002
MANUSCRIPT HANDLED BY DAVID L. BISH